ACS Catalysis

pubs.acs.org/acscatalysis Research Article

Intermediate $Sr_2Co_{1.5}Fe_{0.5}O_{6-\delta}$ Tetragonal Structure between Perovskite and Brownmillerite as a Model Catalyst with Layered Oxygen Deficiency for Enhanced Electrochemical Water Oxidation

Sivasankara Rao Ede, Candyce N. Collins, Carlos D. Posada, Gibin George, Hui Wu, William D. Ratcliff, Yulin Lin, Jianguo Wen, Shubo Han, and Zhiping Luo*

Cite This: *ACS Catal.* 2021, 11, 4327–4337 Read Online

ACCESS | Metrics & More | Article Recommendations | Supporting Information

ABSTRACT: The generation of hydrogen in an environmentally benign way is highly essential to meet future energy demands. However, in the process of splitting water electrochemically, sluggish kinetics of the oxygen evolution reaction (OER) curtails its applicability, as it drags energy input. Herein, we synthesized Sr–Co–Fe–O oxides to optimize their OER activity by varying the Co/Fe ratio. Among them, $Sr_2Co_{1.5}Fe_{0.5}O_{6-\delta}$ exhibited the best OER catalytic activity in the series, with an overpotential of 318 mV at 10 mA cm^{-2} and Tafel slope of 44.8 mV dec^{-1}. High-resolution neutron powder diffraction analysis identified an intermediate structure between the perovskite and brownmillerite, with alternating layers of disorderly orientated oxygen-deficient tetrahedra and fully stoichiometric octahedra. The unique stacking of tetrahedral and octahedral units facilitates desired interactions between the electrode surface and electrolyte. Theoretical calculations revealed that increased covalency of Co 3d and O 2p in $Sr_2Co_{1.5}Fe_{0.5}O_{6-\delta}$ oxide is another primary contributor to its augmented water oxidation ability. As a model for developing catalysts with such an intermediate structure, the synergetic effect of oxygen vacancy and hybridization between Co 3d and O 2p assured the $Sr_2Co_{1.5}Fe_{0.5}O_{6-\delta}$ oxide as a better catalyst for its enhanced OER activity.

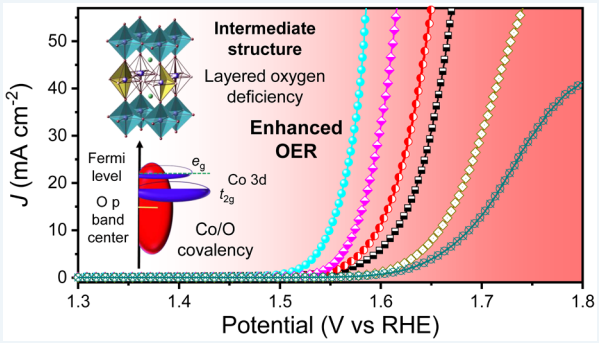

KEYWORDS: *catalyst, crystal structure, oxide, oxygen evolution, perovskite, water splitting*

INTRODUCTION

Development of sustainable ways for energy production is of prime importance, as the depletion of fossil fuels due to overwhelming industrialization and urbanization is increasing exponentially.[1] As an alternate, hydrogen, called as "future fuel", can be made via electrochemical water splitting, which is one of the most promising methods.[2] The produced hydrogen and oxygen from water are actual feeds for fuel cells.[3] In addition, considering metal–air batteries with oxygen reduction reaction (ORR) and oxygen evolution reaction (OER) counterparts, OER shows important manifold applications.[4,5] In the case of OER under alkaline conditions, the intercalation of OH^- ions and O_2 molecules released from the electrode surface forms several intrinsic kinetic barriers, and each of them adds up to the additional overpotentials.[6] When it is an acid and neutral solution, breaking of H_2O molecules still requires surplus energy. To influence the OER at ease, numerous electrocatalysts are investigated to mitigate anodic overpotentials; among them, noble metal-based catalysts, such as IrO_2 and RuO_2, delivered superior performance under corrosive acidic conditions.[6] However, the scarcity and cost associated with these noble metal catalysts limit their broad-scale applications in generating hydrogen for continuous industrial production.[7]

To replace scarce metals, 3d transition metal-based catalysts such as Co, Ni, and Fe with their favorable electronic configurations could deliver promising OER activities and they are earth-abundant too.[8−10] Several perovskites and their derivatives appeared as promising materials for water electrolysis,[11] lithium–air batteries,[12] fuel cells,[13] and photovoltaic applications.[14] In these materials, the structural oxygen stoichiometry plays a pivotal role in diverse applications.[15,16] The properties of ABO_3 perovskites can be tuned by methodically selecting A and B metal cations with desired atomic or ionic radii. Partial replacing or doping of any one of these A, B, and O sites drastically improves their ability in a specific application because of associated changes in their

Received: January 31, 2021
Revised: March 8, 2021
Published: March 23, 2021

respective physical, chemical, and electronic properties.[17] The perovskites with Co, Ni, and Fe on the B site are intensively studied as electrocatalysts for OER and ORR applications.[18] However, the OER activities of perovskites are still limited, and hence, the study in the stoichiometry aspect on the B site and related oxygen is highly recommended to boost them for real-scale applications. Among these B-site metal cations, Co-based perovskite catalysts gained much interest in the research community due to their superior OER activity when Co is coordinated with oxygen atoms octahedrally.

For example, the OER activity of $LaCoO_3$ was enhanced by introducing Fe substitution,[19] which influenced the covalency of Co 3d and O 2p. In another report, different magnitudes of $LaCoO_3$ nanoparticles were analyzed for their OER activity, and the one with ∼80 nm size displayed better OER activity among others.[11] The high catalytic activity of ∼80 nm $LaCoO_3$ particles was attributed to the intermediate spin state of cobalt. In another work, $La_{0.5}Sr_{0.5}CoO_3$ nanotubes were synthesized via the electrospinning method and employed as a bifunctional catalyst for both OER and ORR in Li−O_2, and here, the presence of high surface areas of nanotubes and oxygen vacancies created by Sr doping produced superior OER kinetics.[20] Between $SrCoO_{3-\delta}$[21] and $CaCoO_{3-\delta}$,[21] both catalysts formed cubic crystal structures with the same cobalt species having an intermediate spin state; however, $CaCoO_{3-\delta}$ showed better OER activity due to the presence of oxygen vacancies. The effect of the crystal structure was pronounced in another work. Among electrochemically synthesized $ZnCo_2O_4$ and Co_3O_4, the former one exhibited grander OER performance due to octahedral Co units in the crystal lattice.[22] Recently, brownmillerite-structured Ca_2FeCoO_5 was studied as a highly efficient OER catalyst, and its catalytic activity is attributed to the interplay between Co/Fe in orthorhombic unit cells.[23−26] Density functional theory (DFT) calculations suggest that enhancement of charge transfer between Co/Fe 3d and O 2p orbitals plays a significant role in improving OER activity of Ca_2FeCoO_5 because of random distribution of Co and Fe atoms.[23] Lin et al. recently studied the calcination temperature effect on OER activity of $SrCo_{0.5}Fe_{0.5}O_{3-\delta}$ perovskite.[27] Further insights regarding the Fe substitution of the Co site to tune the electronic properties for improving the OER performance are not reported yet.

Herein, we for the first time elaborate the formulation of a series of Sr−Co−Fe−O oxides by varying the Co/Fe ratio to understand the effect of Fe substitution on OER activity, and $Sr_2Co_{1.5}Fe_{0.5}O_{6-\delta}$ oxide was found to be an efficient OER catalyst. High-resolution neutron powder diffraction (NPD) analysis identified an intermediate structure between perovskite and brownmillerite, with oxygen-deficient tetrahedral units sandwiched between octahedral units. While the OER of this intermediate structure was not reported previously, the unique stacking of tetrahedral and octahedral units facilitates desired interactions between the electrode surface and electrolyte. Theoretical calculations revealed that the increased covalency of Co 3d and O 2p in $Sr_2Co_{1.5}Fe_{0.5}O_{6-\delta}$ oxide is another main contributor to its augmented water oxidation ability. The synergetic effect of oxygen vacancy and hybridization between Co 3d and O 2p assured the $Sr_2Co_{1.5}Fe_{0.5}O_{6-\delta}$ oxide as a better catalyst for the enriched OER activity.

MATERIALS AND METHODS

Materials and Synthesis. Strontium nitrate, cobalt(II) nitrate hexahydrate, iron(III) nitrate nonahydrate, KOH pellets for electrolyte, and citric acid (CA) were purchased from Sigma-Aldrich; ethylenediaminetetraacetic acid (EDTA) and ammonia solution (28−30 vol %) were purchased from VWR International. All chemicals were used without any further purification. The series of $Sr_2Co_{2-x}Fe_xO_{6-\delta}$ oxides were prepared by sol−gel Pechini process using EDTA and CA as chelating agents and by adjusting pH 8−10.[28] Initially, 0.02 M strontium nitrate, the molar ratio of nitrate salts of Co and Fe varies according to the ratio of oxides, and the nitrate salts were dissolved in 75 mL of distilled water and stirred for 30 min on a hotplate at 80 °C. After 30 min, EDTA and CA were added, and then, the pH of the solution was adjusted between 8 and 10 using ammonia solution and allowed to stir for another 30 min. The water was slowly evaporated to form a gel, and this gel was carbonized at 250 °C for 5 h. After carbonization, black powders were collected and annealed at 1050 °C at a ramping rate of 5 °C min^{-1} for 12 h (Figure S1).

Characterizations. The X-ray diffraction (XRD) patterns were recorded using a Rigaku MiniFlex 600 X-ray diffractometer with Cu Kα radiation. Transmission electron microscopy (TEM) elemental analysis was conducted using a FEI Talos F200X TEM/STEM instrument at 200 kV, and high-resolution (HRTEM) imaging was conducted using an Argonne chromatic aberration-corrected TEM (ACAT) FEI Titan 80-300 ST at 200 kV, with a CEOS C_c/C_s corrector to correct both spherical and chromatic aberrations. HRTEM image and electron diffraction (ED) simulations were done using the Tempas program. X-ray photoelectron spectroscopy (XPS) was conducted using the Thermo Scientific ESCALAB 250Xi and Kratos AXIS-ULTRA DLD-600W. NPD was conducted using BT-1 and BT-4 diffractometers at the NIST Center for Neutron Research (NCNR). BT-1 was run using a Cu(311) monochromator at λ = 1.5400 Å, and data were collected in the 2θ range of 3−168° with a step size of 0.05°. The BT-4 was run at 14.7 meV with the following collimations in stream order 60′−40′−80′−100′. Pyrolytic graphite filters were placed before and after the sample. The BET (Brunauer, Emmett, and Teller) surface area measurements were carried out using the Quantachrome SI. The oxygen contents were determined using cerimetric titration.[29] Initially, the concentration of $CeSO_4$ was calculated by standardizing using the known concentration of Mohr's salt. A total of ∼50 mg of $FeCl_2{\cdot}4H_2O$ and ∼25 mg of samples were dissolved in nitrogen gas-purged 3 M (mol/L) HCl solution and then titrated against $CeSO_4$ by adding one drop of ferroin as an indicator, the end point being visually detected from the color change from orange to green.

Electrochemical Measurements. Electrodes were fabricated by coating samples with an approximate loading of 1 mg on carbon cloth using *N*-methyl pyrrolidine with 10% polyvinylidene fluoride as a binder in 0.5 cm^2 area. The surface of carbon cloth was cleaned thoroughly with 30 vol % of ethanol by ultrasonication before they were used as substrates for the electrode. Linear sweep voltammogram (LSV) curves were obtained at a scan rate of 2 mV s^{-1} after conducting five cyclic voltammograms (CVs) at a scan rate of 100 mV s^{-1}. Tafel plots were obtained from LSVs, and electrochemical impedance spectroscopy (EIS) was conducted in the range of 10 kHz to 1 Hz, with an amplitude of 5 mV at an applied potential of 0.72 V versus Hg/HgO reference electrode. All EIS data were fitted using a Randles circuit using the CHI 760E electrochemical workstation (CH Instrument, USA). KOH electrolyte was prepared, and all electrochemical

https://doi.org/10.1021/acscatal.1c00465
ACS Catal. 2021, 11, 4327−4337

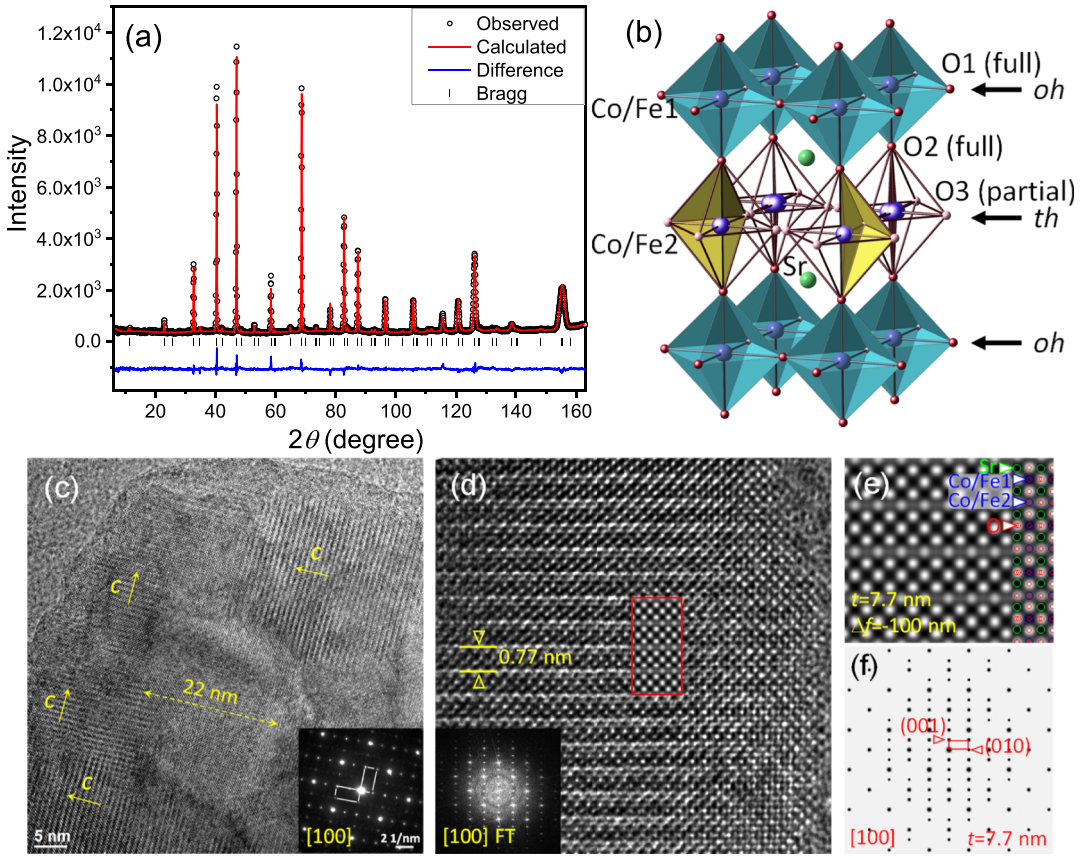

Figure 1. (a) NPD pattern of $Sr_2Co_{1.5}Fe_{0.5}O_{6-\delta}$ oxide; (b) structural model of the intermediate tetragonal phase containing a sequence of alternating octahedral (oh) and tetrahedral (th) layers, where only two randomly orientated tetrahedra are shown for clarity; (c) TEM image showing 90°-twinning domains (insert is an ED pattern); (d) HRTEM image along [100] (insert is an FT pattern and a simulated image); (e) simulated image (thickness t = 7.7 nm and defocus Δf = −100 nm) with overlayed atomic projection; and (f) simulated ED pattern (thickness t = 7.7 nm).

Table 1. NPD Refinement from $Sr_2Co_{1.5}Fe_{0.5}O_{6-\delta}$ at Room Temperature

	Wyckoff site	x	y	z	U_{iso} (×100, Å^2)	site occupation
Sr	2g	0.5	0.5	0.2591(3)	0.93(4)	1.0
Co/Fe 1	1a	0	0	0	0.4(1)	0.774(9)/0.226(9)
Co/Fe 2	4k	−0.023(1)	0.023(1)	0.5	0.6(1)	0.181(2)/0.069(2)
O1	2f	0.5	0	0	2.0(2)	1.0
O2	2g	0	0	0.2422(4)	1.9(2)	1.0
O3	4m	0	0.543(2)	0.5	1.7(2)	0.348(4)

measurements were conducted using plastic vessels to avoid leaching of glass. The same carbon cloth with large dimensions was used as a counter electrode. All data were 100% *IR* (*I* stands for current and *R* stands for resistance)-corrected and shifted to the reversible hydrogen electrode (RHE) scale by calibrating the Hg/HgO reference electrode using the formula $E_{vsRHE} = E_{vsHg/HgO} + E_{øHg/HgO} + 0.059$ pH for OER in 1 M and 3 M (mol/L) KOH. Experiments were conducted on the CHI 760E instrument.

Computational Study. The QUANTUM-ESPRESSO package was used for first-principles calculations through the DFT method.[30] The atomic DOSs for hexagonal $SrCoO_{3-\delta}$ and tetragonal $Sr_2Co_{1.75}Fe_{0.25}O_{6-\delta}$ and $Sr_2Co_{1.5}Fe_{0.5}O_{6-\delta}$ were calculated using the 2 × 2 × 1 supercell. For $SrCo_{0.5}Fe_{0.5}O_{3-\delta}$ cubic perovskite, a 2 × 2 × 2 supercell was used. Integration over the Brillouin zone was carried out using the Monkhorst−Pack scheme with a 2 × 2 × 2 mesh of *k*-points for all phases. The oxygen vacancy was created by deleting one O atom in the supercell near the experimental input value from cerimetry calculations.

RESULTS AND DISCUSSION

Structural Analysis. In the $Sr_2Co_{2-x}Fe_xO_{6-\delta}$ oxide series, when x = 0, the XRD pattern reveals a hexagonal perovskite $SrCoO_{3-\delta}$ as the major phase, which is indexed with JCPDS file no. 48-0875, with a space group of $P6_3/mmc$ (no. 194) and lattice parameters of a = 5.4941 Å and c = 4.2444 Å, and a tetragonal structure as a minor impurity phase, which is indexed with JCPDS file no. 44-1064, with a space group of $P4/m$ (no. 83) and lattice parameters of a = 5.846 Å and c = 7.290 Å (Figure S2). When x = 0.25, 0.5, and 0.75, three oxides with Fe substitution on the Co site ($Sr_2Co_{1.75}Fe_{0.25}O_{6-\delta}$, $Sr_2Co_{1.5}Fe_{0.5}O_{6-\delta}$, and $Sr_2Co_{1.25}Fe_{0.75}O_{6-\delta}$) exhibit a tetragonal structure with a space group of $P4/mmm$ (no. 123),[31] as portrayed in Figure S3a, and a representative pattern from $Sr_2Co_{1.5}Fe_{0.5}O_{6-\delta}$ is shown in Figure S3c. This tetragonal phase

https://doi.org/10.1021/acscatal.1c00465
ACS Catal. 2021, 11, 4327−4337

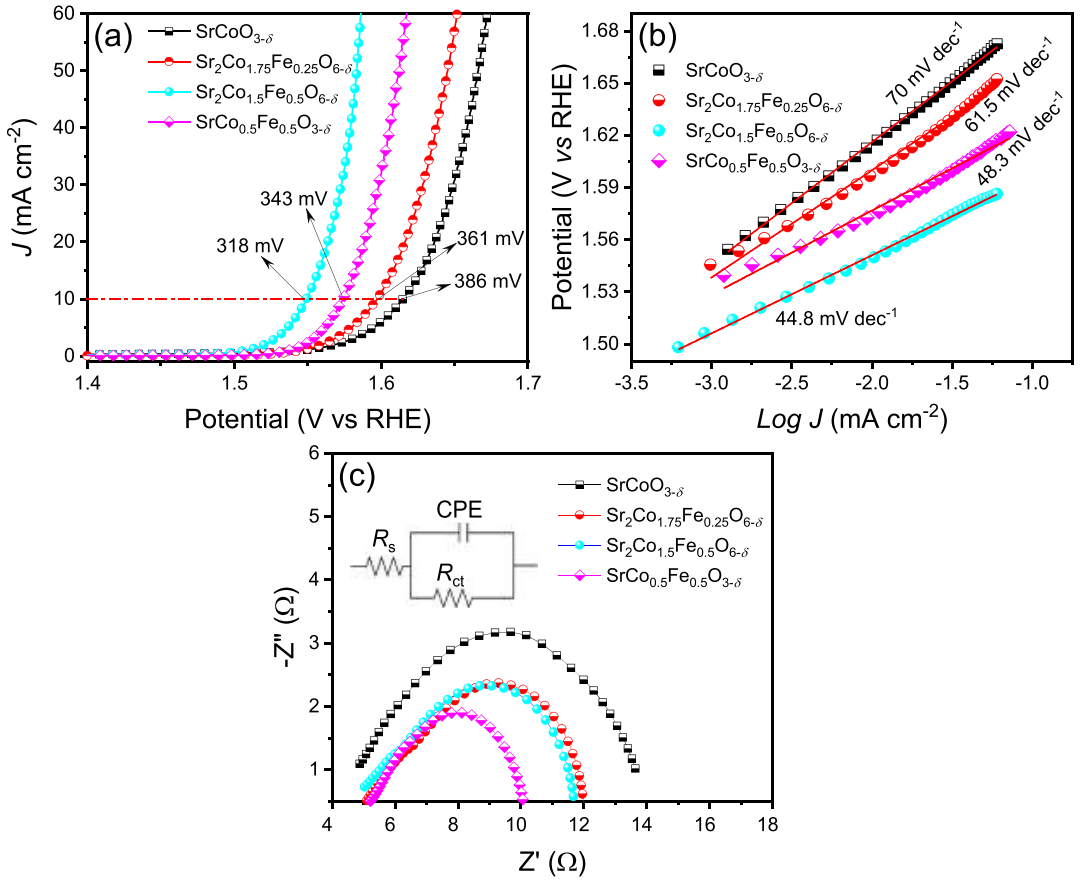

Figure 2. (a) LSV plots; (b) Tafel slopes; and (c) Nyquist plots of $SrCoO_{3-\delta}$, $Sr_2Co_{1.75}Fe_{0.25}O_{6-\delta}$, $Sr_2Co_{1.5}Fe_{0.5}O_{6-\delta}$, and $SrCo_{0.5}Fe_{0.5}O_{3-\delta}$ oxides.

is further refined using NPD below. However, when x = 1−2, the $SrCo_{0.5}Fe_{0.5}O_{3-\delta}$, $SrCo_{0.375}Fe_{0.625}O_{3-\delta}$, $SrCo_{0.25}Fe_{0.75}O_{3-\delta}$, $SrCo_{0.125}Fe_{0.875}O_{3-\delta}$, and $SrFeO_{3-\delta}$ oxides exhibit a simple cubic perovskite structure, with a space group of $Pm\bar{3}m$,[32] as shown in Figure S3b, and a representative pattern from $SrCo_{0.125}Fe_{0.875}O_{3-\delta}$ is shown in Figure S3d. A small superlattice peak appears near 11.5° in the XRD pattern of the tetragonal phase, while it is absent in the patterns of the cubic phase (insets in Figure S3c,d).

The NPD pattern from $Sr_2Co_{1.5}Fe_{0.5}O_{6-\delta}$ oxide collected at room temperature is shown in Figure 1a, and its refined structural parameters are listed in Table 1, with satisfactory weighted profile residal R_{wp} = 0.0620, profile residual R_p = 0.0485, and goodness of fit χ^2 = 1.50. Rietveld refinement reveals that $Sr_2Co_{1.5}Fe_{0.5}O_{6-\delta}$ oxide is tetragonal (space group $P4/mmm$) with lattice parameters of a = 3.8605(1) Å and c = 7.7271(5) Å, which is an intermediate structure between cubic perovskite and othorhombic brownmillerite. This intermediate tetragonal phase contains a sequence of alternating octahedral (oh) and tetrahedral (th) layers (...oh−th−oh−th...), as shown in Figure 1b. The oh layer is composed of corner-shared octahedra $(Co/Fe)O_6$, which is a characteristic of the cubic perovskite structure, and the th layer contains Co/Fe ions surrounded by two apical O^{2-} and two equatorial O^{2-}, which are statistically distributed over four O^{2-} sites. The oxygen occupancy is refined, and its stoichiometric composition is expressed as $Sr_2Co_{1.5}Fe_{0.5}O_{5.392}$. The refined parameters of the NPD pattern are in accordance with cerimetry (Table S1). All Fe-substituted oxides exhibit oxygen deficiency (Table S1).

Figure S4a presents the NPD pattern of $SrCo_{0.5}Fe_{0.5}O_{3-\delta}$ oxide at room temperature, and it is fitted with a simple cubic structure with the $Pm\bar{3}m$ space group. The corresponding refined structural parameters are shown in Table S2, with satisfactory fitting factors. The oxygen occupancy is refined, and its stoichiometry is $Sr(Co_{0.50}Fe_{0.50})O_{2.77}$. In this structure, the oxygen vacancies randomly distribute at any oxygen positions, so that the overall cubic perovskite structure is unchanged.

TEM observation shows that the synthesized samples are composed of nanoparticles, with an average size of ∼80 nm. The nanoparticles are sintered to form particles in ∼μm's during annealing at 1050 °C in the last step of the synthesis. This annealing ensured that single phases were obtained. As shown in Figure 1c, along the [100] orientation, 90°-twinning domains in 20−30 nm are observed, as evidenced from double-spacing lattice fringes. The domain without the double-spacing fringes is [001]-oriented, which is also at 90° with the [100] orientation. These twins may add further oxygen defect sites compared with cubic perovskites without twins. An ED pattern is inserted, showing 90° twins. A magnified HRTEM image is shown in Figure 1d, where atomic layers are revealed. A Fourier transform (FT) pattern is inserted, with the same geometry of the ED pattern. With image simulation, the cationic layers could be identified, as shown in Figure 1e (a simulated image is also inserted in Figure 1d for comparison). The simulated ED pattern in Figure 1f is consistent with the observed ED pattern. Furthermore, STEM EDS mapping of $Sr_2Co_{1.5}Fe_{0.5}O_{6-\delta}$ reveals the uniform distribution of Sr, Co, Fe, and O elements all over the nanoparticles (Figure S5). The

https://doi.org/10.1021/acscatal.1c00465
ACS Catal. 2021, 11, 4327−4337

EDS spectrum, as shown in Figure S5f, confirms the presence of Co and Fe in 3:1 ratio.

OER Study. The LSV plots of Sr−Co−Fe−O oxides are displayed in Figure S6a, and some representative results are shown in Figure 2a, indicating that $Sr_2Co_{1.5}Fe_{0.5}O_{6-\delta}$ oxide has the lowest overpotential of 318 mV at 10 mA cm^{-2}, and the second best is $SrCo_{0.5}Fe_{0.5}O_{3-\delta}$, showing an overpotential of 343 mV for electrochemical water oxidation.

$Sr_2Co_{1.5}Fe_{0.5}O_{6-\delta}$ also demonstrated superior OER kinetics with the Tafel slope value of 44.8 mV dec^{-1} (Figures S6b and 2b). All Fe-substituted oxides exhibit low overpotentials and enhanced OER kinetics, compared with undoped $SrCoO_{3-\delta}$ oxide. The Nyquist plots, fitted with Randle's equivalent circuit, are presented in Figures S6c and 2c. $Sr_2Co_{1.5}Fe_{0.5}O_{6-\delta}$ and $SrCo_{0.5}Fe_{0.5}O_{3-\delta}$ show low charge transfer (R_{ct}) values, compared with $SrCo_{0.5}Fe_{0.5}O_{3-\delta}$ and $Sr_2Co_{1.75}Fe_{0.25}O_{6-\delta}$, which is also reflected in Tafel slope values. However, surprisingly, oxides with higher Fe contents, such as $SrCo_{0.375}Fe_{0.625}O_{3-\delta}$ and $SrCo_{0.125}Fe_{0.875}O_{3-\delta}$, exhibit slightly lower R_{ct} values (Figure S6c and Table S3) than $Sr_2Co_{1.5}Fe_{0.5}O_{6-\delta}$, but they failed to compete due to lower cobalt content in their compositions. We compared our catalyst's OER performance with that of other oxides reported in the literature (Table S4). Our catalyst possesses comparable or even superior properties to those in some of the previous reports.

We conducted BET analysis to understand the synergetic effect of the surface area and oxygen vacancies (Figure S7 and Table S5). We estimated specific activity (Table S5) of all samples by normalizing the current with the BET surface area (J_{BET}). After normalization, $Sr_2Co_{1.5}Fe_{0.5}O_{6-\delta}$ shows the specific activity of 0.00327 mA cm^{-2} BET at 1.55 V, and the activity is much higher than that of other Sr−Co−Fe−O oxides (Table S5). Furthermore, we estimated the electrochemical surface area (ECSA) by calculating electrochemical double-layer capacitance (EDLC) from CVs in the range of 0.1−0.2 V at different scan rates. It was found that $Sr_2Co_{1.5}Fe_{0.5}O_{6-\delta}$ showed the highest EDLC value among all oxides (Figures S8 and S9). The enhanced catalytic activity of $Sr_2Co_{1.5}Fe_{0.5}O_{6-\delta}$ is attributed to its unusual structural arrangement with the presence of oxygen vacancies, which facilitate the maximum interaction between the catalyst and electrolyte.[33]

To get more insights into the electrochemical activity, we conducted XPS analysis. Figure 3 shows Co 2p and Fe 2p high-resolution spectra of all oxides for comparison. Figure 3a presents the Co 2p high-resolution spectra, and the magnified range of 783−777 eV depicting the Co $2p_{3/2}$ region is shown on the right side of Figure 3a.[34] With the increase in Fe content, Co $2p_{3/2}$ chemical line intensity decreases monotonically (Figure 3a). Fe $2p_{3/2}$ chemical line intensity increases (Figure 3b), suggesting that Fe is doped on the Co site.[35] Furthermore, it is found that cobalt chemical lines contain Co^{4+} and Co^{3+} species. Figure S10 displays deconvoluted high-resolution spectra of Co $2p_{3/2}$.[35] Similarly, Fe $2p_{3/2}$ chemical lines also show a similar binding energy value (~710 eV) for all oxides, indicating that Fe is predominantly present in the 3+ oxidation state. As the x value increases, a smaller shift in Fe $2p_{3/2}$ chemical lines is observed toward higher binding energy, suggesting that Fe^{4+} coexists with the Fe^{3+} species, which is also observed from deconvoluted Fe $2p_{3/2}$ chemical lines in high-resolution spectra (Figure S11).[36]

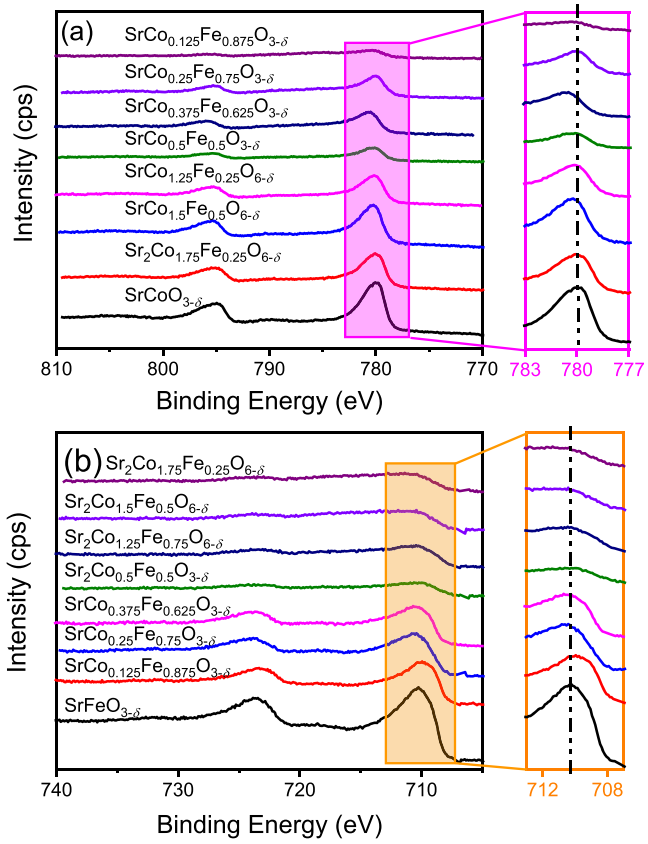

Figure 3. Comparative analysis of oxidation states in Sr−Co−Fe−O oxides. (a) Co 2p high-resolution XPS spectra, with enlargement on the right side showing the Co $2p_{3/2}$ chemical line. (b) Fe 2p high-resolution XPS spectra, with enlargement on the right side showing the Fe $2p_{3/2}$ chemical line.

We observed a change in the ratio of Co^{3+}/Co^{4+} and Fe^{3+}/Fe^{4+} with respect to the change in the Co/Fe ratio, as shown in Figures S10 and S11. The reason for changes could be due to charge disproportion between cobalt and iron centers in the B-site.[37−39] Among all the oxides, $Sr_2Co_{1.5}Fe_{0.5}O_{6-\delta}$ shows a high relative intensity for Co^{4+} (Figure S10b) and Fe^{4+} (Figure. S11d) species. The presence of a high number of Co^{4+} over Co^{3+} improves the OER activity by enhancing the O 2p character in the covalent mixing of the hybrid orbitals Co 3d and O 2p.[21] On the other hand, the presence of a greater number of Fe^{4+} ions could augment the water oxidation ability of the catalyst.[40]

The oxygen vacancies in $Sr_2Co_{1.5}Fe_{0.5}O_{6-\delta}$ are further confirmed by deconvoluting the Sr 3d and O 1s high-resolution spectra (Figure 4). The Sr 3d chemical line is deconvoluted with lattice and surface doublets with an area ratio of 1:1.5, and each is composed of $3d_{3/2}$ and $3d_{5/2}$ (Figure 4a). The doublet with higher binding energies indicates the surface Sr species (SrO or $Sr(OH)_2$), which are formed due to surface termination of oxides.[41−43] Another doublet with a lower binding energy represents the lattice Sr. Figure 4b presents the O 1s spectrum, which is fitted with three peaks: one at a higher binding energy and two at lower binding energies (<531 eV). The peak at the higher binding energy consists of surface and adsorbed oxygen.[44,45] The two peaks presented at lower binding energies denote the lattice oxygen.[46,47] When the oxide surface is enriched with Sr by forming SrO or $Sr(OH)_2$, oxygen defects are formed, Sr + O

https://doi.org/10.1021/acscatal.1c00465
ACS Catal. 2021, 11, 4327−4337

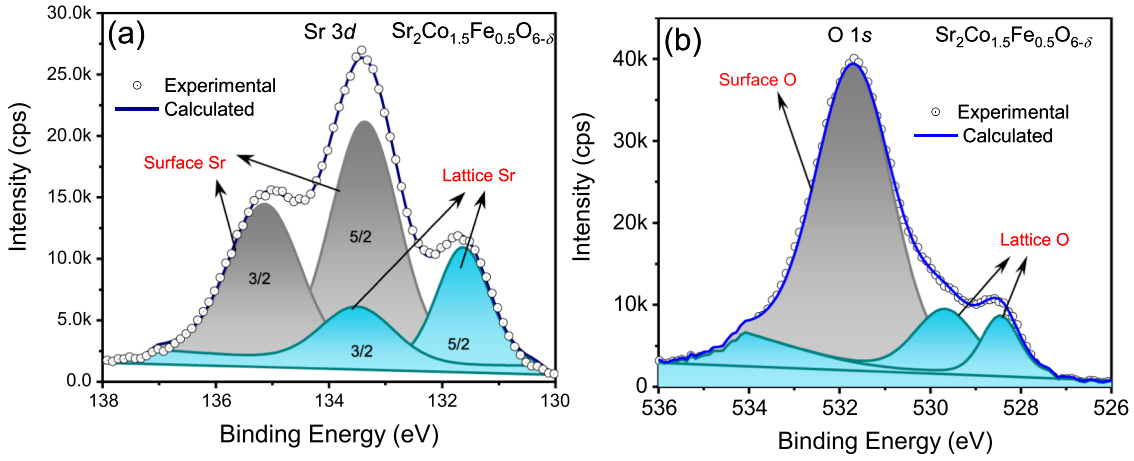

Figure 4. Deconvoluted Sr 3d (a) and O 1s (b) XPS spectra of $Sr_2Co_{1.5}Fe_{0.5}O_{6-\delta}$ oxide.

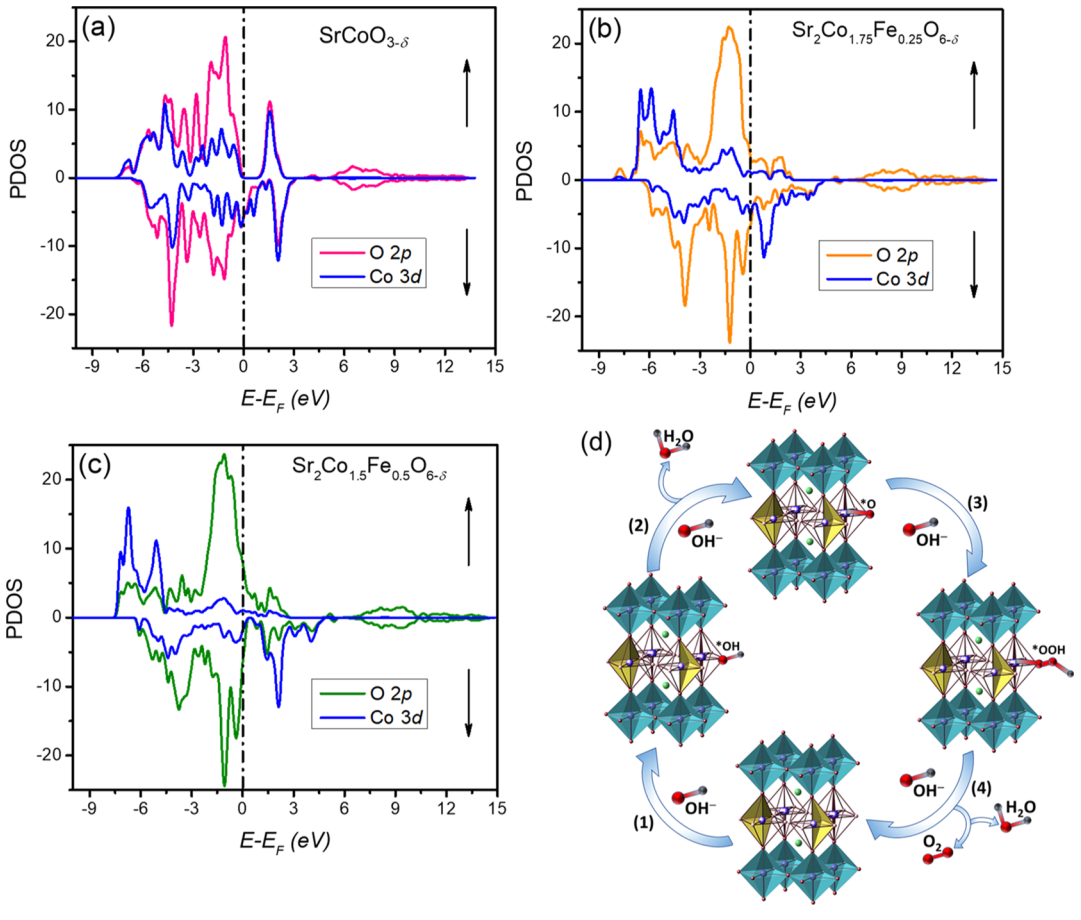

Figure 5. PDOS of the Co 3d and O 2p for $SrCoO_{3-\delta}$ (a), $Sr_2Co_{1.75}Fe_{0.25}O_{6-\delta}$ (b), and $Sr_2Co_{1.5}Fe_{0.5}O_{6-\delta}$ (c) oxides (dotted vertical line indicates the Fermi level and arrows represent the spin-up and spin-down of spin projection); and (d) schematic illustration of the approach between OH^- and oxygen vacancies of $Sr_2Co_{1.5}Fe_{0.5}O_{6-\delta}$ oxide.

$\leftrightarrow$ SrO + $V_O^{\bullet\bullet}$ + $V_{Sr}^{\bullet\bullet}$, which is consistent with the oxygen content estimation from cerimetry and NPD results.[48] Here, $V_O^{\bullet\bullet}$ stands for oxygen vacancy and $V_{Sr}^{\bullet\bullet}$ stands for strontium vacancy. The presence of oxygen defects enhances the molecular porosity of the oxide and improves the adsorption ability of OER intermediates such as *O, *OH, and *OOH. In addition, we also deconvoluted the Sr 3d and O 1s high-resolution spectra to reveal the presence of oxygen vacancies (Figure S12). The deconvoluted results suggest that all oxides exhibit the oxygen defects. The increase in lattice oxygen with the x value further confirms the presence of the Fe^{4+} species (Figure S12).[36]

The OER process can proceed through two different pathways, that is, lattice oxygen mechanism (LOM) or adsorbate evolution mechanism (AEM).[49] In the LOM pathway, the lattice oxygen should be able to escape via interacting with adsorbed oxygen (*O) by leaving deficiencies in the lattice, acting as a new active site. In the AEM pathway,

https://doi.org/10.1021/acscatal.1c00465
ACS Catal. 2021, 11, 4327−4337

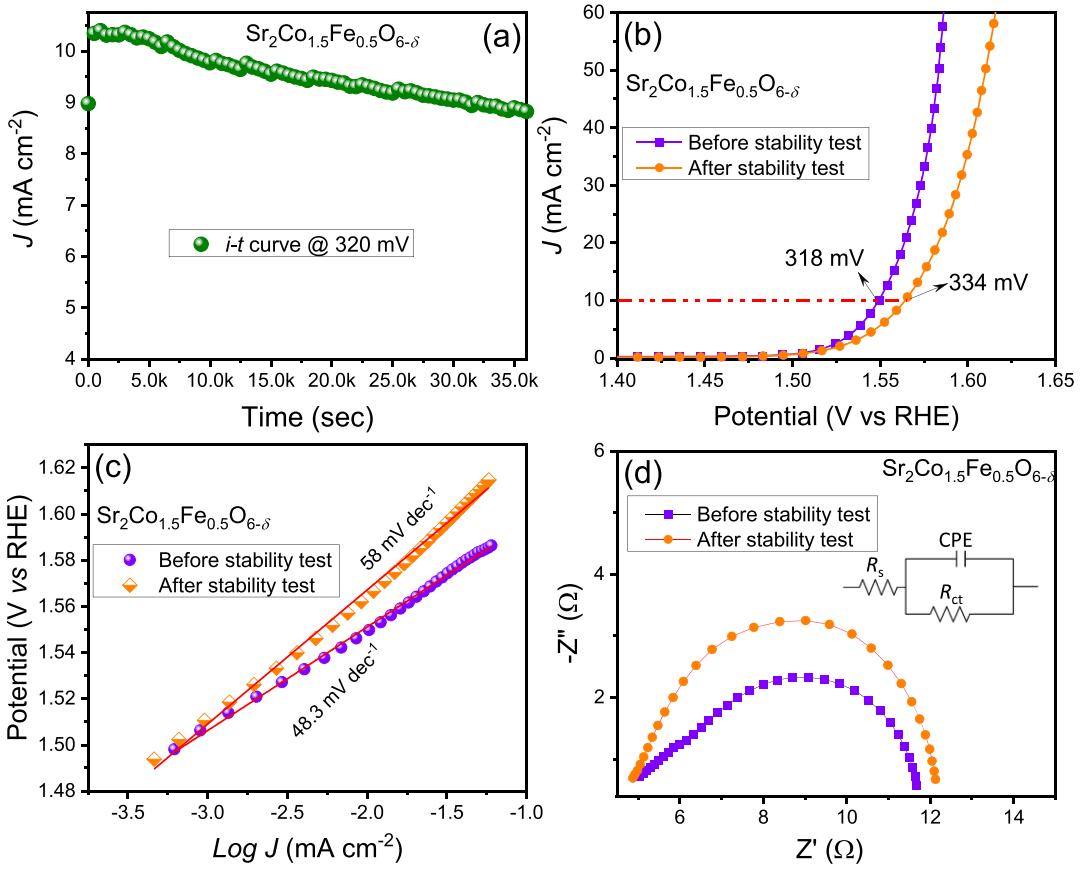

Figure 6. (a) Stability test of $Sr_2Co_{1.5}Fe_{0.5}O_{6-\delta}$ oxide at 1.550 V vs RHE for 10 h; (b) LSV plots; (c) Tafel slopes; and (d) Nyquist plots before and after stability test.

the reactant (OH^-) generates OER intermediates such as *OH, *O, and *OOH at the anode surface by donating electrons and evolves oxygen gas. Nevertheless, in both pathways during the electrochemical process, intralattice charge transfer occurs, which could result in local charge redistribution.[50] Energetically, the covalency of oxygen orbitals and cation orbitals depends on their relative positions. Electrons transfer from cations to oxygen during electrochemical reaction if the oxygen energy level is below the energy level of cations, which restricts the escape of incoming oxygen from the lattice and leads to the exclusion of lattice oxygen. However, if the oxygen orbitals are above those of the cation *d*-center, a reduction in charge of oxygen occurs via electron transfer from oxygen to nearby cations. The reduced oxygen quickly escapes from the lattice because of a high degree of freedom. Hence, both energy levels of oxygen and cations should be evaluated to estimate the OER mechanism and covalency.[51]

DFT Calculation. Disproportionation of the B-site in perovskite oxides[40] or Fe into the lattice of perovskite oxides[27] significantly improves the covalency of oxygen and cations. Yagi et al. reported the improved OER activity of Fe^{4+}-based quadruple perovskite $CaCu_3Fe_4O_{12}$ because of the formation of a covalent bonding network due to incorporation of Cu^{2+} and Fe^{4+}.[40] Wang et al. synthesized $SrCo_{0.5}Fe_{0.5}O_{3-\delta}$ cubic perovskite at different calcinating temperatures (600, 800, 1000, and 1200 °C) and evaluated their OER performance.[27] The perovskite prepared at 800 °C showed excellent OER activity, and DFT studies reveal that improved covalency of O 2p and Co 3d is a key for high catalytic activity. However, a change in the crystal structure of Sr-based perovskites by varying the Co/Fe ratio at the B-site was not reported.

Here, we carried out the DFT calculations for $SrCoO_{3-\delta}$, $Sr_2Co_{1.75}Fe_{0.25}O_{6-\delta}$, $Sr_2Co_{1.5}Fe_{0.5}O_{6-\delta}$, and $SrCo_{0.5}Fe_{0.5}O_{3-\delta}$ oxides to correlate the covalent mixing of Co 3d and O 2p orbitals with their OER activity. The total density of states (TDOS) is shown in Figure S13, and projected density of states (PDOS) is shown in Figures 5a–c and S14. High orbital mixing is observed in the TDOS of $Sr_2Co_{1.5}Fe_{0.5}O_{6-\delta}$ oxide at the Fermi level (E_F) cross-over compared with that of other three compounds (Figure S13). The PDOS of Co 3d and ligand O 2p of $SrCoO_{3-\delta}$ oxide is depicted in Figure 5a, which shows a negative overlap at E_F, whereas the PDOS of Fe-doped $Sr_2Co_{1.75}Fe_{0.25}O_{6-\delta}$, $Sr_2Co_{1.5}Fe_{0.5}O_{6-\delta}$, and $SrCo_{0.5}Fe_{0.5}O_{3-\delta}$ oxides displays Co(e_g)−O(p)-enhanced intermixing at E_F cross-over (Figures 5b,c and S14). $Sr_2Co_{1.5}Fe_{0.5}O_{6-\delta}$ shows superior intermixing compared to $Sr_2Co_{1.75}Fe_{0.25}O_{6-\delta}$ and $SrCo_{0.5}Fe_{0.5}O_{3-\delta}$. The increased intermixing signifies the stronger covalency of Co 3d and O 2p orbitals. This covalency directly scales with the binding energy of oxygen,[19] oxygen vacancy formation energy,[52,53] and the energy barrier associated with electron transfer in OER.[54] Therefore, the superior covalency is one of the reasons for enhanced OER activity of $Sr_2Co_{1.5}Fe_{0.5}O_{6-\delta}$ along with having the intermediate tetragonal structure. Figure 5d depicts the role of oxygen vacancy in the catalytic activity. Initially, the oxygen-deficient sites facilitate facile kinetics for OH^- to interact with the $(CoFe)O_6$ subunit, which makes the OER kinetics much faster.[21,55,56] The synergetic effect of oxygen vacancy and covalency (Figure 5c) makes the $Sr_2Co_{1.5}Fe_{0.5}O_{6-\delta}$ perovskite a

https://doi.org/10.1021/acscatal.1c00465
ACS Catal. 2021, 11, 4327−4337

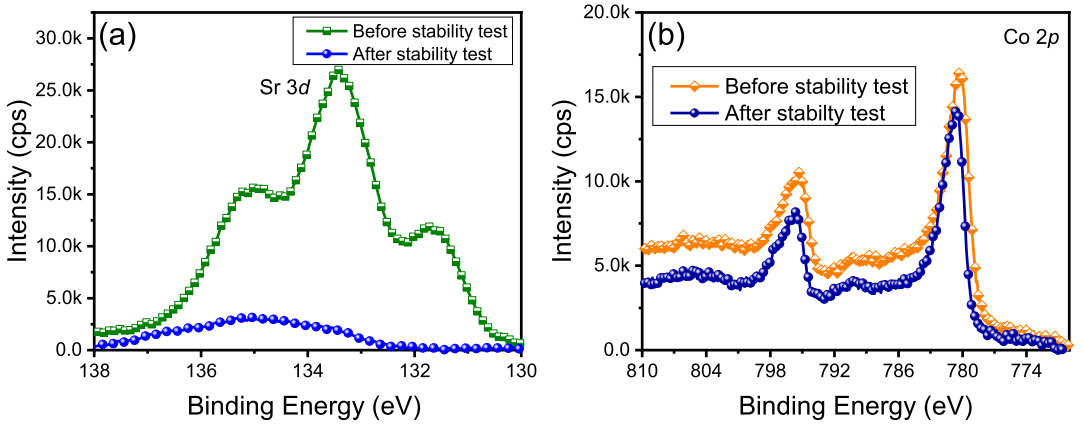

Figure 7. (a) Sr 3d chemical lines and (b) Co 2p chemical lines of $Sr_2Co_{1.5}Fe_{0.5}O_{6-\delta}$ before and after stability test.

better candidate for electrochemical water splitting,[21] which serves as a model for developing other catalysts with such a unique intermediate structure.

Recently, Majee et al. synthesized a perovskite with the stoichiometric formula $La_{0.699}Sr_{0.301}Co_{0.702}Fe_{0.298}O_{3-\delta}$ by annealing at 750, 975, and 1200 °C having a cubic crystal structure. They observed that the LSCF oxide prepared at 975 °C temperature shows superior activity in electrochemical water oxidation. Theoretical studies suggest that there is a decrease in E_F with an increase in annealing temperature and LSCF-975 °C has an optimized desirable E_F for the adsorption and desorption of OER intermediates.[57] Nakayama et al. observed enhanced OER activity in the brownmillerite structure of Ca_2FeCoO_5 specifically prepared at 1100 °C than in the same sample prepared at lower temperatures because of enrichment of cobalt in tetrahedral sites, which is predicted theoretically.[58] Chen et al. studied the change in OER activity by creating cationic vacancies in perovskite hydroxide $SnCo_{0.9}Fe_{0.1}(OH)_6$ (SnCoFe) nanocubes. They found that SnCoFe nanocubes treated for 10 min showed enhanced OER activity compared to others. Theoretical analysis suggests the formation of Sn vacancies that improve the desorption ability of the O* intermediates.[59] In our case, the presence of oxygen vacancies in the intermediate tetragonal structure results in tetrahedral pyramidal structure that optimizes the E_F, which in turn helps in facilitating facile adsorption and desorption of OER intermediates during the OER process.

Long-Term Stability. Furthermore, the stability of $Sr_2Co_{1.5}Fe_{0.5}O_{6-\delta}$ oxide is examined at 1.550 V versus RHE for 10 h (Figure 6a). It shows good stability over time and slight deterioration of activity with a 16 mV increase in overpotential (Figure 6b). The Tafel slopes and Nyquist plots before and after the stability test are in accordance with the LSV curves (Figure 6c,d). The decreased activity of $Sr_2Co_{1.5}Fe_{0.5}O_{6-\delta}$ oxide could be attributed to the formation of low-conductive amorphous Co_3O_4 from octahedral Co units on the surface because of leaching of Sr under extreme OER conditions.[60]

The Sr leaching was confirmed using the XPS analysis (Figures 7 and Figure. S15) along with STEM EDS mapping (Figure S16). The XPS chemical line of Sr 3d after the stability test displays a considerable decrease in its intensity, unlike Co 2p, Fe 2p, and O 1s chemical lines (Figures 7b and S15). The XPS spectrum of Co 2p shows a slight shift in its binding energy (~0.5 eV) toward higher binding energy, which could be attributed to structural transformation on the catalyst surface during the OER stability test. This facile way of fabricating the OER catalyst with optimum oxygen vacancies paves an attractive way to explore other oxides for superior OER catalytic activity.

In addition, we have compared the activity of our catalyst with that of commercial IrO_2 (Figure S17). It was found that our catalyst $Sr_2Co_{1.5}Fe_{0.5}O_{6-\delta}$ showed comparatively better OER activity with an overpotential of 318 mV, while commercial IrO_2 showed 331 mV @ 10 mA cm^{-2}; our catalyst had enhanced stability with a loss of ~15% activity, while commercial IrO_2 had a loss of ~30% activity in 10 h.

From the abovementioned observations, it is possible to synthesize compounds with such an intermediate structure in other systems with lattice oxygen defects for interacting with OER intermediates, achieving high-rate OER and high-scale stability in an alkaline environment for further studies in various applications.

CONCLUSIONS

A series of Sr−Co−Fe−O oxides have been synthesized and evaluated for OER. We have identified $Sr_2Co_{1.5}Fe_{0.5}O_{6-\delta}$ with an intermediate structure between cubic perovskite and brownmillerite with layered oxygen deficiency, as a promising catalyst for enhanced OER activities, with the lowest overpotential of 318 mV at 10 mA cm^{-2} and with a Tafel slope value of 44.8 mV dec^{-1}. The superior activity of $Sr_2Co_{1.5}Fe_{0.5}O_{6-\delta}$ is attributed to its layered oxygen-deficient structure and increased covalency of Co 3d and O 2p. This unique structure with layered oxygen deficiency and increased covalency provides a model for designing advanced OER catalysts with improved hydrogen production performance for less energy input.

ASSOCIATED CONTENT

Supporting Information

The Supporting Information is available free of charge at https://pubs.acs.org/doi/10.1021/acscatal.1c00465.

Sample synthesis, XRD, NPD, TEM, XPS, BET, electrochemical study, DFT calculation, cerimetry analysis, comparison with other catalysts in the literature, oxygen stoichiometry calculation using cerimetry titration, and crystallographic data (PDF)

https://doi.org/10.1021/acscatal.1c00465
ACS Catal. 2021, 11, 4327−4337

AUTHOR INFORMATION

Corresponding Author

Zhiping Luo − *Department of Chemistry, Physics and Materials Science, Fayetteville State University, Fayetteville, North Carolina 28301, United States;* orcid.org/0000-0002-8264-6424; Email: zluo@uncfsu.edu

Authors

Sivasankara Rao Ede − *Department of Chemistry, Physics and Materials Science, Fayetteville State University, Fayetteville, North Carolina 28301, United States*

Candyce N. Collins − *Department of Chemistry, Physics and Materials Science, Fayetteville State University, Fayetteville, North Carolina 28301, United States*

Carlos D. Posada − *Department of Chemistry, Physics and Materials Science, Fayetteville State University, Fayetteville, North Carolina 28301, United States*

Gibin George − *Department of Chemistry, Physics and Materials Science, Fayetteville State University, Fayetteville, North Carolina 28301, United States*

Hui Wu − *NIST Center for Neutron Research, National Institute of Standards and Technology, Gaithersburg, Maryland 20899, United States*

William D. Ratcliff − *NIST Center for Neutron Research, National Institute of Standards and Technology, Gaithersburg, Maryland 20899, United States; Department of Materials Science and Engineering, University of Maryland, College Park, Maryland 20742, United States*

Yulin Lin − *Center for Nanoscale Materials, Argonne National Laboratory, Lemont, Illinois 60439, United States*

Jianguo Wen − *Center for Nanoscale Materials, Argonne National Laboratory, Lemont, Illinois 60439, United States;* orcid.org/0000-0002-3755-0044

Shubo Han − *Department of Chemistry, Physics and Materials Science, Fayetteville State University, Fayetteville, North Carolina 28301, United States*

Complete contact information is available at: https://pubs.acs.org/10.1021/acscatal.1c00465

Author Contributions

S.R.E. conducted the sample synthesis, XPS, electrochemical measurements, and DFT and prepared the manuscript; C.N.C. and C.D.P. conducted the sample processing and preparation; G.G. analyzed the data; H.W. and W.D.R. conducted NPD and refinement at NIST; Y.L. and J.W. conducted the TEM work at ANL; S.H. conducted chemical analysis; and Z.L. designed and supervised the experiment, analyzed data, and revised the manuscript.

Notes

The authors declare no competing financial interest.

The identification of any commercial product or trade name does not imply endorsement or recommendation by the National Institute of Standards and Technology.

ACKNOWLEDGMENTS

This research was support by the U.S. Nation Science Foundation (NSF) DMR 1827731. The Center for High-Resolution Neutron Scattering (CHRNS) is a national user facility jointly funded by the NIST Center for Neutron Research (NCNR) and the NSF DMR 1508249. Use of the Center for Nanoscale Materials, an Office of Science user facility, was supported by the U.S. Department of Energy, Office of Science, Office of Basic Energy Sciences, under contract no. DE-AC02-06CH11357.

REFERENCES

(1) Moriarty, P.; Honnery, D. What Is the Global Potential for Renewable Energy? *Renewable Sustainable Energy Rev.* **2012**, *16*, 244−252.

(2) Tee, S. Y.; Win, K. Y.; Teo, W. S.; Koh, L.-D.; Liu, S.; Teng, C. P.; Han, M.-Y. Recent Progress in Energy-Driven Water Splitting. *Adv. Sci.* **2017**, *4*, 1600337.

(3) Debe, M. K. Electrocatalyst Approaches and Challenges for Automotive Fuel Cells. *Nature* **2012**, *486*, 43−51.

(4) Cheng, F.; Chen, J. Metal−Air Batteries: From Oxygen Reduction Electrochemistry to Cathode Catalysts. *Chem. Soc. Rev.* **2012**, *41*, 2172−2192.

(5) Anantharaj, S.; Kundu, S. Do the Evaluation Parameters Reflect Intrinsic Activity of Electrocatalysts in Electrochemical Water Splitting? *ACS Energy Lett.* **2019**, *4*, 1260−1264.

(6) Hu, C.; Zhang, L.; Gong, J. Recent Progress Made in the Mechanism Comprehension and Design of Electrocatalysts for Alkaline Water Splitting. *Energy Environ. Sci.* **2019**, *12*, 2620−2645.

(7) Zeng, K.; Zhang, D. Recent Progress in Alkaline Water Electrolysis for Hydrogen Production and Applications. *Prog. Energy Combust. Sci.* **2010**, *36*, 307−326.

(8) Fabbri, E.; Habereder, A.; Waltar, K.; Kötz, R.; Schmidt, T. J. Developments and Perspectives of Oxide-Based Catalysts for the Oxygen Evolution Reaction. *Catal. Sci. Technol.* **2014**, *4*, 3800−3821.

(9) Sankar, S. S.; Karthick, K.; Sangeetha, K.; Gill, R. S.; Kundu, S. Annexation of Nickel Vanadate ($Ni_3V_2O_8$) Nanocubes on Nanofibers: An Excellent Electrocatalyst for Water Oxidation. *ACS Sustainable Chem. Eng.* **2020**, *8*, 4572−4579.

(10) Anantharaj, S.; Karthick, K.; Murugan, P.; Kundu, S. V^{3+} Incorporated β-$Co(OH)_2$: A Robust and Efficient Electrocatalyst for Water Oxidation. *Inorg. Chem.* **2020**, *59*, 730−740.

(11) Zhou, S.; Miao, X.; Zhao, X.; Ma, C.; Qiu, Y.; Hu, Z.; Zhao, J.; Shi, L.; Zeng, J. Engineering Electrocatalytic Activity in Nanosized Perovskite Cobaltite through Surface Spin-State Transition. *Nat. Commun.* **2016**, *7*, 11510.

(12) Yang, W.; Salim, J.; Li, S.; Sun, C.; Chen, L.; Goodenough, J. B.; Kim, Y. Perovskite $Sr_{0.95}Ce_{0.05}CoO_{3-\delta}$ Loaded with Copper Nanoparticles as a Bifunctional Catalyst for Lithium-Air Batteries. *J. Mater. Chem.* **2012**, *22*, 18902−18907.

(13) Zhou, Y.; Guan, X.; Zhou, H.; Ramadoss, K.; Adam, S.; Liu, H.; Lee, S.; Shi, J.; Tsuchiya, M.; Fong, D. D.; Ramanathan, S. Strongly Correlated Perovskite Fuel Cells. *Nature* **2016**, *534*, 231−234.

(14) Mefford, J. T.; Rong, X.; Abakumov, A. M.; Hardin, W. G.; Dai, S.; Kolpak, A. M.; Johnston, K. P.; Stevenson, K. J. Water Electrolysis on $La_{1-x}Sr_xCoO_{3-\delta}$ Perovskite Electrocatalysts. *Nat. Commun.* **2016**, *7*, 11053.

(15) George, G.; Jackson, S. L.; Luo, C. Q.; Fang, D.; Luo, D.; Hu, D.; Wen, J.; Luo, Z. Effect of Doping on the Performance of High-Crystalline $SrMnO_3$ Perovskite Nanofibers as a Supercapacitor Electrode. *Ceram. Int.* **2018**, *44*, 21982−21992.

(16) George, G.; Ede, S. R.; Luo, Z. *Fundamentals of Perovskite Oxides: Synthesis, Structure, Properties and Applications*; CRC Press, 2020.

(17) Ji, Q.; Bi, L.; Zhang, J.; Cao, H.; Zhao, X. S. The Role of Oxygen Vacancies of ABO_3 Perovskite Oxides in the Oxygen Reduction Reaction. *Energy Environ. Sci.* **2020**, *13*, 1408−1428.

(18) Vij, V.; Sultan, S.; Harzandi, A. M.; Meena, A.; Tiwari, J. N.; Lee, W.-G.; Yoon, T.; Kim, K. S. Nickel-Based Electrocatalysts for Energy-Related Applications: Oxygen Reduction, Oxygen Evolution, and Hydrogen Evolution Reactions. *ACS Catal.* **2017**, *7*, 7196−7225.

(19) Duan, Y.; Sun, S.; Xi, S.; Ren, X.; Zhou, Y.; Zhang, G.; Yang, H.; Du, Y.; Xu, Z. J. Tailoring the Co 3d-O 2p Covalency in $LaCoO_3$ by Fe Substitution To Promote Oxygen Evolution Reaction. *Chem. Mater.* **2017**, *29*, 10534−10541.

(20) Liu, G.; Chen, H.; Xia, L.; Wang, S.; Ding, L.-X.; Li, D.; Xiao, K.; Dai, S.; Wang, H. Hierarchical Mesoporous/Macroporous

Perovskite $La_{0.5}Sr_{0.5}CoO_{3-x}$ Nanotubes: A Bifunctional Catalyst with Enhanced Activity and Cycle Stability for Rechargeable Lithium Oxygen Batteries. *ACS Appl. Mater. Interfaces* **2015**, *7*, 22478−22486.
(21) Li, X.; Wang, H.; Cui, Z.; Li, Y.; Xin, S.; Zhou, J.; Long, Y.; Jin, C.; Goodenough, J. B. Exceptional Oxygen Evolution Reactivities on $CaCoO_3$ and $SrCoO_3$. *Sci. Adv.* **2019**, *5*, No. eaav6262.
(22) Kim, T. W.; Woo, M. A.; Regis, M.; Choi, K.-S. Electrochemical Synthesis of Spinel Type $ZnCo_2O_4$ Electrodes for Use as Oxygen Evolution Reaction Catalysts. *J. Phys. Chem. Lett.* **2014**, *5*, 2370−2374.
(23) Yamada, I.; Kinoshita, M.; Oda, S.; Tsukasaki, H.; Kawaguchi, S.; Oka, K.; Mori, S.; Ikeno, H.; Yagi, S. Enhanced Catalytic Activity and Stability of the Oxygen Evolution Reaction on Tetravalent Mixed Metal Oxide. *Chem. Mater.* **2020**, *32*, 3893−3903.
(24) Thundiyil, S.; Kurungot, S.; Devi, R. N. Bifunctional Oxygen Reduction and Evolution Activity in Brownmillerites $Ca_2Fe_{1-x}Co_xO_5$. *ACS Omega* **2019**, *4*, 31−38.
(25) Kowalski, D.; Kiuchi, H.; Motohashi, T.; Aoki, Y.; Habazaki, H. Activation of Catalytically Active Edge-Sharing Domains in Ca_2FeCoO_5 for Oxygen Evolution Reaction in Highly Alkaline Media. *ACS Appl. Mater. Interfaces* **2019**, *11*, 28823−28829.
(26) Tsuji, E.; Motohashi, T.; Noda, H.; Kowalski, D.; Aoki, Y.; Tanida, H.; Niikura, J.; Koyama, Y.; Mori, M.; Arai, H.; Ioroi, T.; Fujiwara, N.; Uchimoto, Y.; Ogumi, Z.; Habazaki, H. Brownmillerite-Type Ca_2FeCoO_5 as a Practicable Oxygen Evolution Reaction Catalyst. *ChemSusChem* **2017**, *10*, 2864−2868.
(27) Lin, Q.; Zhu, Y.; Hu, Z.; Yin, Y.; Lin, H.-J.; Chen, C.-T.; Zhang, X.; Shao, Z.; Wang, H. Boosting the Oxygen Evolution Catalytic Performance of Perovskites via Optimizing Calcination Temperature. *J. Mater. Chem. A* **2020**, *8*, 6480−6486.
(28) Cho, S. G.; Johnson, P. F.; Condrate, R. A. Thermal Decomposition of (Sr, Ti) Organic Precursors during the Pechini Process. *J. Mater. Sci.* **1990**, *25*, 4738−4744.
(29) Karppinen, M.; Matvejeff, M.; Salomäki, K.; Yamauchi, H. Oxygen Content Analysis of Functional Perovskite-Derived Cobalt Oxides. *J. Mater. Chem.* **2002**, *12*, 1761−1764.
(30) Giannozzi, P.; Baroni, S.; Bonini, N.; Calandra, M.; Car, R.; Cavazzoni, C.; Ceresoli, D.; Chiarotti, G. L.; Cococcioni, M.; Dabo, I.; Dal Corso, A.; de Gironcoli, S.; Fabris, S.; Fratesi, G.; Gebauer, R.; Gerstmann, U.; Gougoussis, C.; Kokalj, A.; Lazzeri, M.; Martin-Samos, L.; Marzari, N.; Mauri, F.; Mazzarello, R.; Paolini, S.; Pasquarello, A.; Paulatto, L.; Sbraccia, C.; Scandolo, S.; Sclauzero, G.; Seitsonen, A. P.; Smogunov, A.; Umari, P.; Wentzcovitch, R. M. QUANTUM ESPRESSO: A Modular and Open-Source Software Project for Quantum Simulations of Materials. *J. Phys.: Condens. Matter* **2009**, *21*, 395502.
(31) Belenkaya, I. V.; Matvienko, A. A.; Nemudry, A. P. In Situ High-Temperature Diffraction Study of the Perovskite-Brownmillerite Phase Transition in $SrCo_{0.8}Fe_{0.2}O_{2.5}$ in Isostoichiometric Mode. *Dokl. Phys. Chem.* **2014**, *459*, 185−189.
(32) Nakatsuka, A.; Yoshiasa, A.; Nakayama, N.; Mizota, T.; Takei, H. Oxygen-Deficient Strontium Cobaltate, $SrCoO_{2.64}$. *Acta Crystallogr., Sect. C: Cryst. Struct. Commun.* **2004**, *60*, i59−i60.
(33) Kim, J.; Yin, X.; Tsao, K.-C.; Fang, S.; Yang, H. $Ca_2Mn_2O_5$ as Oxygen-Deficient Perovskite Electrocatalyst for Oxygen Evolution Reaction. *J. Am. Chem. Soc.* **2014**, *136*, 14646−14649.
(34) McIntyre, N. S.; Cook, M. G. X-Ray Photoelectron Studies on Some Oxides and Hydroxides of Cobalt, Nickel, and Copper. *Anal. Chem.* **1975**, *47*, 2208−2213.
(35) Huang, Y.; Zhao, B.; Ang, R.; Lin, S.; Huang, Z.; Tan, S.; Liu, Y.; Song, W.; Sun, Y. Enhanced Thermoelectric Performance and Room-Temperature Spin-State Transition of Co^{4+} Ions in the $Ca_3Co_{4-x}Rh_xO_9$ System. *J. Phys. Chem. C* **2013**, *117*, 11459−11470.
(36) Ghaffari, M.; Shannon, M.; Hui, H.; Tan, O. K.; Irannejad, A. Preparation, Surface State and Band Structure Studies of $SrTi_{1-x}Fe_xO_{3-\delta}$ (x=0−1) Perovskite-Type Nano Structure by X-Ray and Ultraviolet Photoelectron Spectroscopy. *Surf. Sci.* **2012**, *606*, 670−677.
(37) Hawn, D. D.; DeKoven, B. M. Deconvolution as a Correction for Photoelectron Inelastic Energy Losses in the Core Level XPS Spectra of Iron Oxides. *Surf. Interface Anal.* **1987**, *10*, 63−74.
(38) Hosaka, Y.; Ichikawa, N.; Saito, T.; Manuel, P.; Khalyavin, D.; Attfield, J. P.; Shimakawa, Y. Two-Dimensional Charge Disproportionation of the Unusual High Valence State Fe^{4+} in a Layered Double Perovskite. *J. Am. Chem. Soc.* **2015**, *137*, 7468−7473.
(39) Jiang, L.; Saldana-Greco, D.; Schick, J. T.; Rappe, A. M. Enhanced Charge Ordering Transition in Doped $CaFeO_3$ through Steric Templating. *Phys. Rev. B: Condens. Matter Mater. Phys.* **2014**, *89*, 235106.
(40) Yagi, S.; Yamada, I.; Tsukasaki, H.; Seno, A.; Murakami, M.; Fujii, H.; Chen, H.; Umezawa, N.; Abe, H.; Nishiyama, N.; Mori, S. Covalency-Reinforced Oxygen Evolution Reaction Catalyst. *Nat. Commun.* **2015**, *6*, 8249.
(41) Vasquez, R. P. X-Ray Photoelectron Spectroscopy Study of Sr and Ba Compounds. *J. Electron Spectrosc. Relat. Phenom.* **1991**, *56*, 217−240.
(42) van der Heide, P. A. W. Systematic X-Ray Photoelectron Spectroscopic Study of $La_{1-x}Sr_x$-Based Perovskite-Type Oxides. *Surf. Interface Anal.* **2002**, *33*, 414−425.
(43) Crumlin, E. J.; Mutoro, E.; Liu, Z.; Grass, M. E.; Biegalski, M. D.; Lee, Y.-L.; Morgan, D.; Christen, H. M.; Bluhm, H.; Shao-Horn, Y. Surface Strontium Enrichment on Highly Active Perovskites for Oxygen Electrocatalysis in Solid Oxide Fuel Cells. *Energy Environ. Sci.* **2012**, *5*, 6081−6088.
(44) Norman, C.; Leach, C. In Situ High Temperature X-Ray Photoelectron Spectroscopy Study of Barium Strontium Iron Cobalt Oxide. *J. Membr. Sci.* **2011**, *382*, 158−165.
(45) Uwamino, Y.; Ishizuka, T.; Yamatera, H. X-Ray Photoelectron Spectroscopy of Rare-Earth Compounds. *J. Electron Spectrosc. Relat. Phenom.* **1984**, *34*, 67−78.
(46) Galenda, A.; Natile, M. M.; Krishnan, V.; Bertagnolli, H.; Glisenti, A. LaSrCoFeO and Fe_2O_3/LaSrCoFeO Powders: Synthesis and Characterization. *Chem. Mater.* **2007**, *19*, 2796−2808.
(47) Foix, D.; Sathiya, M.; McCalla, E.; Tarascon, J.-M.; Gonbeau, D. X-ray Photoemission Spectroscopy Study of Cationic and Anionic Redox Processes in High-Capacity Li-Ion Battery Layered-Oxide Electrodes. *J. Phys. Chem. C* **2016**, *120*, 862.
(48) Wang, X.; Huang, K.; Qian, J.; Cong, Y.; Ge, C.; Feng, S. Enhanced CO Catalytic Oxidation by Sr Reconstruction on the Surface of $La_xSr_{1-x}CoO_{3-\delta}$. *Sci. Bull.* **2017**, *62*, 658.
(49) Rong, X.; Parolin, J.; Kolpak, A. M. A Fundamental Relationship between Reaction Mechanism and Stability in Metal Oxide Catalysts for Oxygen Evolution. *ACS Catal.* **2016**, *6*, 1153−1158.
(50) Zhou, Y.; Sun, S.; Xi, S.; Duan, Y.; Sritharan, T.; Du, Y.; Xu, Z. J. Superexchange Effects on Oxygen Reduction Activity of Edge-Sharing $[Co_xMn_{1-x}O_6]$ Octahedra in Spinel Oxide. *Adv. Mater.* **2018**, *30*, 1705407.
(51) Sun, Y.; Liao, H.; Wang, J.; Chen, B.; Sun, S.; Ong, S. J. H.; Xi, S.; Diao, C.; Du, Y.; Wang, J.-O.; Breese, M. B. H.; Li, S.; Zhang, H.; Xu, Z. J. Covalency Competition Dominates the Water Oxidation Structure−Activity Relationship on Spinel Oxides. *Nat. Catal.* **2020**, *3*, 554−563.
(52) Rossmeisl, J.; Qu, Z.-W.; Zhu, H.; Kroes, G.-J.; Nørskov, J. K. Electrolysis of Water on Oxide Surfaces. *J. Electroanal. Chem.* **2007**, *607*, 83−89.
(53) Hwang, J.; Rao, R. R.; Giordano, L.; Katayama, Y.; Yu, Y.; Shao-Horn, Y. Perovskites in Catalysis and Electrocatalysis. *Science* **2017**, *358*, 751−756.
(54) Sabatier, P. Hydrogénations et Déshydrogénations Par Catalyse. *Ber. Dtsch. Chem. Ges.* **1911**, *44*, 1984−2001.
(55) Suntivich, J.; May, K. J.; Gasteiger, H. A.; Goodenough, J. B.; Shao-Horn, Y. A Perovskite Oxide Optimized for Oxygen Evolution Catalysis from Molecular Orbital Principles. *Science* **2011**, *334*, 1383−1385.
(56) Bockris, J. O. M.; Otagawa, T. The Electrocatalysis of Oxygen Evolution on Perovskites. *J. Electrochem. Soc.* **1984**, *131*, 290.

https://doi.org/10.1021/acscatal.1c00465
ACS Catal. 2021, 11, 4327−4337

(57) Majee, R.; Chakraborty, S.; Salunke, H. G.; Bhattacharyya, S. Maneuvering the Physical Properties and Spin States To Enhance the Activity of La−Sr−Co−Fe−O Perovskite Oxide Nanoparticles in Electrochemical Water Oxidation. *ACS Appl. Energy Mater.* **2018**, *1*, 3342−3350.
(58) Nakayama, K.; Ishikawa, R.; Kuwabara, A.; Kobayashi, S.; Motohashi, T.; Shibata, N.; Ikuhara, Y. Transition-Metal Distribution in Brownmillerite Ca_2FeCoO_5. *Inorg. Chem.* **2019**, *58*, 10209−10216.
(59) Chen, D.; Qiao, M.; Lu, Y. R.; Hao, L.; Liu, D.; Dong, C. L.; Li, Y.; Wang, S. Preferential Cation Vacancies in Perovskite Hydroxide for the Oxygen Evolution Reaction. *Angew. Chem., Int. Ed.* **2018**, *57*, 8691−8696.
(60) Seitz, L. C.; Dickens, C. F.; Nishio, K.; Hikita, Y.; Montoya, J.; Doyle, A.; Kirk, C.; Vojvodic, A.; Hwang, H. Y.; Norskov, J. K.; Jaramillo, T. F. A Highly Active and Stable $IrO_x/SrIrO_3$ Catalyst for the Oxygen Evolution Reaction. *Science* **2016**, *353*, 1011−1014.

https://doi.org/10.1021/acscatal.1c00465
ACS Catal. 2021, 11, 4327−4337